

1  
2  
3  
4  
5  
6  
7  
8  
9  
10  
11  
12  
13  
14  
15  
16  
17  
18  
19  
20  
21  
22

# Multisite Phosphorylation and Binding Alter Conformational Dynamics of the 4E-BP2 Protein

Spencer Smyth<sup>1,2,\*</sup>, Zhenfu Zhang<sup>1,2,\*</sup>, Alaji Bah<sup>3,+</sup>, Thomas E. Tsangaris<sup>2</sup>, Jennifer Dawson<sup>3,\$</sup>,  
Julie D. Forman-Kay<sup>3,4</sup>, and Claudiu C. Gradinaru<sup>1,2,#</sup>

<sup>1</sup>Department of Physics, University of Toronto, Toronto, Ontario, M5S 1A7, Canada;

<sup>2</sup>Department of Chemical & Physical Sciences, University of Toronto Mississauga, Mississauga, Ontario, L5L 1C6, Canada; <sup>3</sup>Program in Molecular Medicine, The Hospital for Sick Children, Toronto, ON M5G 0A4, Canada; <sup>4</sup>Department of Biochemistry, University of Toronto, Toronto, ON M5S 1A8, Canada

\* These authors contributed equally to this work

+ Present address: Department of Biochemistry and Molecular Biology, SUNY Upstate Medical University, Syracuse, NY 13210, United States

\$ Present address: Genomic Medicine Institute, Cleveland Clinic, Cleveland, OH 44195, United States

# Author to whom correspondence may be addressed: [claudiu.gradinaru@utoronto.ca](mailto:claudiu.gradinaru@utoronto.ca)

**KEYWORDS:** IDP, single-molecule fluorescence, anisotropy decay, PET-FCS, smFRET

## 23 **ABSTRACT**

24           Intrinsically disordered proteins (IDPs) play critical roles in regulatory protein interactions,  
25 but detailed structural/dynamics characterization of their ensembles remain challenging, both in  
26 isolation and they form dynamic ‘fuzzy’ complexes. Such is the case for mRNA cap-dependent  
27 translation initiation, which is regulated by the interaction of the predominantly folded eukaryotic  
28 initiation factor 4E (eIF4E) with the intrinsically disordered eIF4E binding proteins (4E-BPs) in a  
29 phosphorylation-dependent manner. Single-molecule Förster resonance energy transfer showed  
30 that the conformational changes of 4E-BP2 induced by binding to eIF4E are non-uniform along  
31 the sequence; while a central region containing both motifs that bind to eIF4E expands and  
32 becomes stiffer, the C-terminal region is less affected. Fluorescence anisotropy decay revealed a  
33 nonuniform segmental flexibility around six different labelling sites along the chain. Dynamic  
34 quenching of these fluorescent probes by intrinsic aromatic residues measured via fluorescence  
35 correlation spectroscopy report on transient intra- and inter-molecular contacts on ns- $\mu$ s  
36 timescales. Upon hyperphosphorylation, which induces folding of ~40 residues in 4E-BP2, the  
37 quenching rates decreased at labelling sites closest to the phosphorylation sites and within the  
38 folded domain, and increased at the other sites. The chain dynamics around sites in the C-terminal  
39 region far away from the two binding motifs were significantly reduced upon binding to eIF4E,  
40 suggesting that this region is also involved in the highly dynamic 4E-BP2:eIF4E complex. Our  
41 time-resolved fluorescence data paint a sequence-level rigidity map of three states of 4E-BP2  
42 differing in phosphorylation or binding status and distinguish regions that form contacts with  
43 eIF4E. This study adds complementary structural and dynamics information to recent studies of  
44 4E-BP2, and it constitutes an important step towards a mechanistic understanding of this important  
45 IDP via integrative modelling.

## 46 INTRODUCTION

47 Intrinsically disordered proteins (IDPs) are a class of proteins that lack well-defined three-  
48 dimensional structures while still carrying out biological functions (1-3). IDPs play a crucial role  
49 in mediating interactions with multiple partners and often function as protein interaction hubs (4,  
50 5). IDPs within these protein complexes can undergo disorder-to-order transitions or remain  
51 dynamic (6). The lack of stable folded structures observed in IDPs leads to the simplistic  
52 assumption that IDPs resemble random coils. In fact, IDPs have transient secondary and tertiary  
53 structures and preferential backbone torsion angle propensities due to electrostatic and other  
54 interactions based on their amino acid sequence, and exhibit a wide range of compactness (6-9).

55 Cap-dependent initiation of translation is regulated by the interaction of eukaryotic  
56 initiation factor 4E (eIF4E) with disordered eIF4E binding proteins (4E-BPs) in a phosphorylation-  
57 dependent manner (10-12). The eIF4E protein, which binds the 7-methyl guanosine cap structure  
58 of mRNA at the 5' end, has been shown to be an oncogene and be involved in the induction of  
59 cellular transformation (13, 14). The eIF4G, a scaffolding protein, plays a crucial role in docking  
60 and assembling several components of the translation initiation machinery at the 5' cap of mRNA  
61 to recruit the ribosome (15). The 4E-BP2 protein is involved in controlling cell growth and  
62 proliferation via regulating mRNA translation (16) and in immunity to viral infections (17). Neural  
63 4E-BP2 also functions in regulating synaptic plasticity, playing an essential role in learning and  
64 memory, and has been implicated in autism spectrum disorder (18, 19).

65 The interaction between eIF4E and eIF4G is the fundamental step that initiates the  
66 translation process. This interaction involves the canonical binding helix-forming YxxxxL $\phi$  motif  
67 of eIF4G, which is also found in all 4E-BPs, binding to the same convex interface of eIF4E. Thus,  
68 the 4E-BPs regulate translation by competing with eIF4G to prevent the assembly of the eIF4F

69 complex and the subsequent mRNA recruitment to the ribosome. Binding of IDPs often leads to  
70 ordering, and transient helical structure around the canonical YxxxxL $\phi$  motif is stabilized upon  
71 eIF4E binding. However, the 4E-BP2:eIF4E complex has been shown by NMR to be highly  
72 dynamic with an exchanging bipartite interface (20), in which the secondary binding site  
73 <sup>78</sup>IPGTV<sup>82</sup> interacts with the lateral surface of eIF4E, as revealed by an X-ray crystal structure  
74 capturing a snapshot of the complex (21).

75         The 4E-BP2 protein is hierarchically phosphorylated. Modification of the first two sites  
76 T37 and T46 results in the hypo-phosphorylated state(22); this 2-site phosphorylation (2P) induces  
77 formation of a 4-stranded  $\beta$ -sheet structure from residues 18-62, partially sequestering the  
78 canonical binding motif and weakening eIF4E binding but still enabling competition with  
79 eIF4G(12). Additional phosphorylation at S65, T70, and S83 leading to a 5-site (5P) state stabilizes  
80 the fold (23), further decreasing the eIF4E affinity and allowing translation initiation to proceed  
81 (10). The disordered region C-terminal to the folded domain (C-IDR) remains disordered after  
82 phosphorylation and stabilizes the folded domain via long-range interactions (12, 23). However,  
83 important details of the structure and dynamics of 4E-BP2 and the eIF4E:4E-BP2 complex remain  
84 unknown, which prevent a clear mechanistic picture of the function of 4E-BP2 and its  
85 phosphoregulation of translation initiation.

86         Typically, IDPs have a wide range of interchanging conformations, therefore obtaining  
87 dynamic information is critically important for understanding their biological functions. Single-  
88 molecule fluorescence (SMF) techniques have been applied previously to measure the  
89 conformational heterogeneity, the global dimensions, and the dynamics of IDPs (24, 25). Here, we  
90 used fluorescence anisotropy decay (FAD) and fluorescence correlation spectroscopy (FCS) to  
91 characterize global and local peptide chain motions in 4E-BP2 upon multisite phosphorylation and

92 upon binding to eIF4E. FCS and FAD are sensitive to chain motions on the nanosecond-to-  
93 microsecond time scale, which is highly relevant for protein folding and for IDP dynamics (26).  
94 FAD measurements informed on the local, segmental flexibility of the peptide chain at various  
95 sites of the protein, leading to a coarse rigidity map of 4E-BP2 in the NP, 5P and eIF4E-bound  
96 states. Using FCS, we resolved up to three different timescales of intra-molecular conformational  
97 dynamics in 4E-BP2 under non-phosphorylated (NP), 5-site-phosphorylated (5P) and denaturing  
98 conditions. In addition, we obtained kinetic information (amplitude and lifetime) of key inter-  
99 molecular contacts of the dynamic binding interface between NP 4E-BP2 and eIF4E.

100       Single-molecule Förster resonance energy transfer (smFRET) measurements of two  
101 different regions of the protein delineated changes in intramolecular distances and chain rigidity  
102 upon multisite phosphorylation, and upon binding to eIF4E. Surprisingly, smFRET showed an  
103 increase in the distance between residues 32 and 91 upon phosphorylation, despite folding-induced  
104 compaction of residues 18 to 62 (12). While in complex with eIF4E, a region of 4E-BP2 containing  
105 both canonical and secondary binding sites expands and stiffens considerably, while the C-terminal  
106 region expands only slightly but remains highly flexible. Our multifaceted SMF characterization  
107 of the 4E-BP2 conformational dynamics is an important step towards understanding the interplay  
108 between folding and release of binding to eIF4E, and it provides valuable information for  
109 calculating conformational ensembles of this multistate IDP via integrative modelling.

110

## 111 **RESULTS AND DISCUSSION**

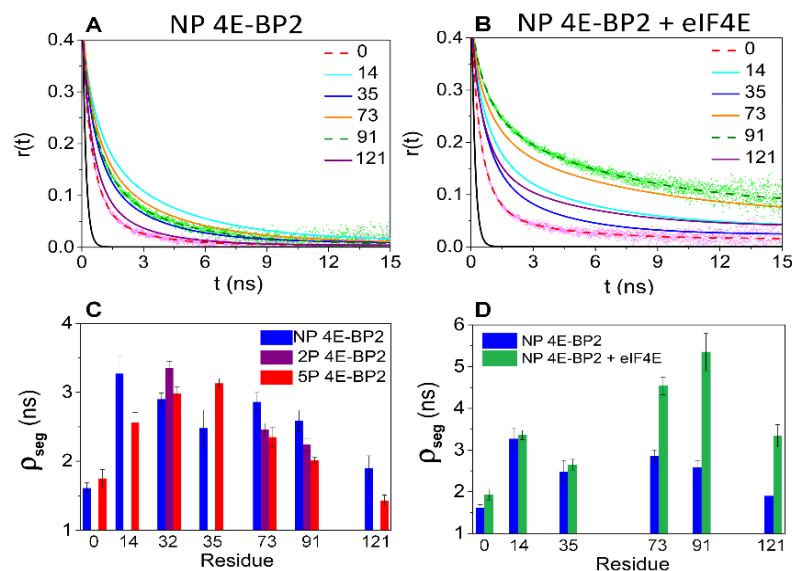
### 112 **Local chain dynamics measured by FAD**

113       The structural flexibility of IDPs is essential for regulating their interactions with other  
114 proteins and their role in signaling processes (3). FAD measures the rotational dynamics of the

115 emission dipole of a fluorophore and is therefore a suitable reporter of the local (segmental) chain  
116 flexibility around the labelling site. Inferred parameters from FAD analysis relate to the spatial  
117 confinement and the friction experienced by the dye, the movement of a protein segment around  
118 the labelling site, and the hydrodynamic radius of the protein segment (27). Probing local  
119 conformational dynamics is particularly relevant for IDPs, for which motions of different segments  
120 may be uncorrelated and obscured by the averaged global dynamics.

121 Six single-cysteine 4E-BP2 constructs were used for site-specific fluorescence labelling:  
122 C0 (i.e., C0ins/C35S/C73S mutations), C14 (S14C/C35S/C73S), C35 (C73S), C73 (C35S), C91  
123 (C35S/C73S/S91C), and C121 (C35S/C73S/C121ins) (**Fig. S1, Table S1**). While the fastest, sub-  
124 ns FAD lifetime ( $\rho_{dye}$ ) typically describes the rotation of the dye-linker around the labelling site,  
125 in IDPs with transient structure the slowest FAD lifetime describes the rotational diffusion of a  
126 protein segment ( $\rho_{seg}$ ), where individual segments can rotate independently(28, 29). Alternatively,  
127 for folded proteins the slowest FAD lifetime describes the rotational diffusion of the entire  
128 protein.(30)

129 **Fig. 1A** shows a family of FAD curves of NP 4E-BP2 with the fluorophore attached to  
130 each of the six different mutated cysteine sites. As dye-protein interactions are expected to be  
131 negligible for Atto 488 (31) (**Fig. S3**), the variations in the anisotropy decays indicate that the  
132 chain flexibility is site/region dependent. FAD fitting parameters using **Eq. 1** (see Methods) are  
133 listed in **Table 1**, for each labelling site and each sample condition. **Fig. 1C** shows a comparison  
134 between segmental lifetimes ( $\rho_{seg}$ ) around each 4E-BP2 labelling site in different phosphorylation  
135 states, i.e., NP, 2P and 5P. These values range from 1.4 ns to 3.4 ns and vary considerably with  
136 the labelling site and with the phosphorylation state.



137

138 **Figure 1.** Fluorescence anisotropy decay (FAD) data for 4E-BP2 fit to Eq. 1. The 4E-BP2 protein was  
 139 labelled with Atto 488 at positions 0, 14, 35, 73, 91 and 121 along the sequence, as described in the text.  
 140 NP 4E-BP2 anisotropy data and fitted curves for all six labelling sites are shown in the absence (A) and in  
 141 the presence of 1  $\mu$ M of eIF4E (B); for reference the FAD of the free dye is shown in black in both panels.  
 142 (C) The slowest rotational lifetime ( $\rho_{seg}$ ) obtained by fitting FAD curves at each labelling site for NP (blue),  
 143 2P (purple) and 5P (red) 4E-BP2. (D) The slowest rotational lifetime ( $\rho_{seg}$ ) obtained by fitting FAD curves  
 144 at each labelling site for NP 4E-BP2 in the absence (blue) and in the presence of (green) of eIF4E.

145

146 **Table 1.** Anisotropy decay parameters for phosphorylated/bound 4E-BP2 states labelled at different sites<sup>a</sup>.

	<i>5P 4E-BP2</i>		<i>2P 4E-BP2</i>		<i>NP 4E-BP2</i>		<i>NP 4E-BP2 + eIF4E</i>	
	$\rho_{dye}$	$\rho_{seg}$ (a)	$\rho_{dye}$	$\rho_{seg}$ (a)	$\rho_{dye}$	$\rho_{seg}$ (a)	$\rho_{dye}$	$\rho_{seg}$ (a)
<i>C0</i>	0.53 ns	1.75 ns (0.72)	-	-	0.51 ns	1.61 ns (0.66)	0.52 ns	1.93 ns (0.70)
<i>S14C</i>	0.56 ns	2.56 ns (0.51)	-	-	0.64 ns	3.27 ns (0.42)	0.62 ns	3.36 ns (0.49)
<i>H32C</i>	0.34 ns	2.98 ns (0.59)	0.41 ns	3.35 ns (0.49)	0.35 ns	2.90 ns (0.55)	-	-
<i>C35</i>	0.55 ns	3.13 ns (0.41)	-	-	0.64 ns	2.48 ns (0.52)	0.62 ns	2.65 ns (0.51)
<i>C73</i>	0.55 ns	2.35 ns (0.54)	0.39 ns	2.46 ns (0.60)	0.62 ns	2.86 ns (0.47)	0.61 ns	4.54 ns (0.46)
<i>S91C</i>	0.57 ns	2.01 ns (0.51)	0.33 ns	2.24 ns (0.66)	0.61 ns	2.59 ns (0.50)	0.65 ns	5.35 ns (0.43)
<i>C121</i>	0.52 ns	1.43 ns (0.61)	-	-	0.53 ns	1.90 ns (0.60)	0.59 ns	3.34 ns (0.59)

147 <sup>a</sup> All data were fit to **Eq. 1** to estimate two rotational correlation lifetimes (dye & segment) and their fractions ( $a$  is the  
148 fraction of the slowest component). Fitting error margins are on the order of  $\pm 0.1$  ns for the lifetimes and  $\pm 0.05$  for  
149 amplitudes (**Table S2**).  
150

151 Many IDPs are more compact than an ideal statistical coil of the same length due to  
152 transient intra-molecular contacts (7, 8, 32). Slower segmental dynamics in PBS buffer (pH 7.4,  
153 140 mM NaCl) was observed than in chemical denaturant (6M GdmCl) at all labelling sites (**Table**  
154 **S2**). The chemically denatured NP and 5P states of 4E-BP2 have similar segmental flexibility  
155 signatures, with  $\rho_{seg} = 0.8 - 0.9$  ns at the ends and  $\rho_{seg} = 1.3 - 1.6$  ns at internal sites. The  
156 values and the trend here match previous measurements for denatured proteins and the  
157 expectations for a random coil state(27, 29). Additionally, the pattern of FAD lifetimes is  
158 consistent overall with that of  $^{15}\text{N}$  relaxation rates(20) and of  $^1\text{H}$ - $^{15}\text{N}$  nuclear Overhauser effect  
159 (NOE) values (12). This suggests that FAD-measured segmental dynamics can probe transient  
160 secondary structure and non-random chain contacts, and reports on the local degree of disorder in  
161 IDPs.

162 Another contribution to the heterogeneous segmental flexibility is the amino acid  
163 composition around each labelling site, with glycine and serine being the most flexible, and  
164 proline, isoleucine and valine the most rigid (33). With 4 Ser and 2 Gly among the first 10 residues,  
165 the N-terminus is the most flexible region of NP 4E-BP2. Considering a 10-residue window, the  
166 positions 14, 73 and 91 are flanked by several rigid residues (Pro, Ile, Val) and the protein appears  
167 to be much less flexible in these regions. The slowest rotational lifetime was observed at position  
168 14 ( $\rho_{seg} = 3.27$  ns), which, in addition to two Pro residues, has two positively charged Arg  
169 residues in its proximity, which may rigidify the segment further via electrostatic interactions.

170 In previous NMR studies, we have shown that a region of 4E-BP2 (residues 18 to 62) folds  
171 upon phosphorylation, while the rest of the chain remains disordered (12). We used FAD to probe



172 the changes in segmental flexibility of 4E-BP2 that are induced by partial (2P) and full (5P)  
173 phosphorylation (**Fig. 1C, Table 1**). The rotational lifetime ( $\rho_{seg}$ ) increases at position 35 (and  
174 only slightly at 32, located within a long loop), while it decreases at all the other dye positions,  
175 which are outside the folded domain, indicating that the chain becomes more flexible. This is  
176 consistent with the formation of the four-stranded beta-sheet fold between residues 18-62 and with  
177 the C-terminal region remaining disordered after phosphorylation. From an entropic perspective,  
178 increased conformational flexibility near the secondary binding site (residues 78 to 82) may also  
179 contribute to decreasing the affinity for eIF4E.

180 FAD has been used previously to quantify and differentiate local binding constants of IDPs  
181 in the context of multisite interactions (28) . **Fig. 1B** shows anisotropy decay data and fitted curves  
182 for the 4E-BP2:eIF4E complex at each of the six labeling sites on 4E-BP2. In contrast with the  
183 apo sample, these curves decay to significantly higher asymptotic values ( $r_{inf}$ , **Table S2**), indicating  
184 that the local motions around each labeling site in 4E-BP2 are hindered after binding to eIF4E.  
185 The largest changes in chain flexibility occur at three C-terminal sites while the changes observed  
186 in the N-terminal sites are minor (**Fig. 1D**). At positions 73, 91 and 121, the segmental rotational  
187 lifetime  $\rho_{seg}$  nearly doubles, from 2-3 ns in the apo state to 4-5 ns in the bound state. Similarly,  
188 rotational freedom of the probe as measured by the half-cone angle,  $\theta$  (**Eq. 2**), is significantly  
189 reduced at the C-terminal labelling sites (**Fig. S2**).

190 Positions 73 and 91 are located near the secondary binding site while position 121 is far  
191 from either binding site but the changes in lifetime are consistent with binding-induced changes to  
192 NMR intensity ratios(20), which demonstrate complete broadening for residues 45-88, significant  
193 broadening for residues 34-90, and broadening at residue 120. The data for positions 73 and 91  
194 likely reflect favorable interactions at the secondary binding site, as well as potentially the

195 competitive interaction of the secondary binding region with the disordered N-terminus of eIF4E  
196 that has been suggested to act as a negative regulator.(34) The NMR broadening results for position  
197 120 together with these FAD data on position 121 support a picture of the 4E-BP2:eIF4E dynamic  
198 complex involving a more extensive part of the C-terminus.

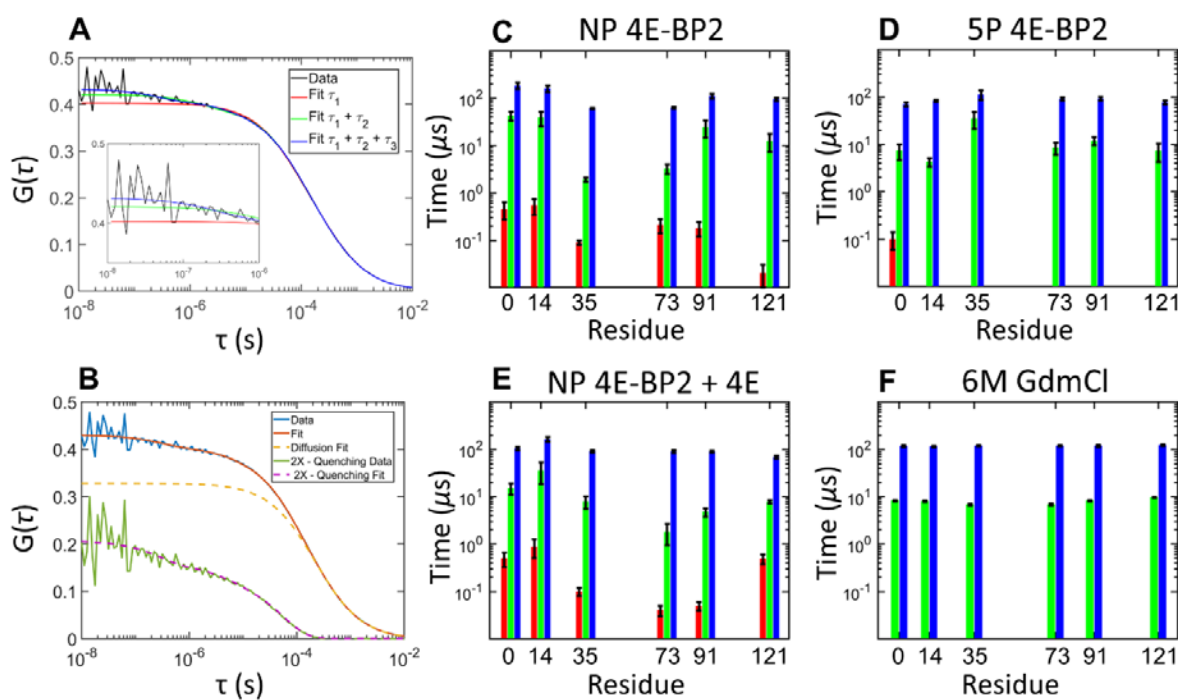
199 The results demonstrate that segmental motion parameters measured by FAD can be used  
200 to disentangle the binding contributions of different regions in an intrinsically disordered protein  
201 as it interacts with its binding partners. More specifically, the changes in  $\theta$  are anti-correlated with  
202 the changes in  $\rho_{seg}$ , indicating that the rotational freedom of the probe and the segmental dynamics  
203 of 4E-BP2 are hindered in the bound state.

#### 204 **Non-local chain dynamics in 4E-BP2 measured by PET-FCS**

205 The same Atto488-labelled 4E-BP2 constructs used for FAD (**Fig. S1, Table S1**) were also  
206 used for FCS experiments. FCS is sensitive to intensity fluctuations caused by the diffusion of the  
207 labelled protein and by the photophysics of the fluorophore (**Eq. 3**). Notably, the fluorophore can  
208 be dynamically quenched by aromatic amino acids via photoinduced electron transfer (PET)(35,  
209 36). Tryptophan (Trp) and tyrosine (Tyr) are the strongest PET quenchers, with a quenching range  
210 of 5-10 Å for typical fluorophores (37, 38). The two tyrosines in the 4E-BP2 sequence (Y34 and  
211 Y54) are most likely acting as quenchers in our FCS measurements.

212 **Fig. 2A-B** shows experimental FCS data, fitting curves, and residuals for a representative  
213 sample, 4E-BP2 labelled with Atto488 at position 73, in the NP state. Models with one diffusion  
214 component and two or three (faster) kinetic components (**Eq. 3**) satisfactorily fit the experimental  
215 autocorrelation decays measured for all 4E-BP2 samples. The (sub-diffusion) kinetic components  
216 in FCS data are attributed to intrinsic triplet-state kinetics of the probe and to dynamic PET  
217 quenching induced by the protein environment.

218 The FCS lifetimes obtained by fitting the data to **Eq. 3** can be grouped into three timescales:  
 219  $\tau_1 \approx 50\text{-}500$  ns,  $\tau_2 \approx 3\text{-}30$   $\mu\text{s}$ , and  $\tau_3 \approx 100$   $\mu\text{s}$ , respectively (**Fig. 2, Table 2**). Conversely, the free  
 220 dye exhibits a single kinetic component with a lifetime of  $12.9 \pm 1.1$   $\mu\text{s}$  (**Fig. S2**), which is similar  
 221 to a previously reported triplet lifetime of Atto488.(39) Thus, for 4E-BP2, the  $\tau_1$  and  $\tau_3$  lifetimes  
 222 are attributed to PET quenching of the dye due to conformational dynamics of the protein, while  
 223 the  $\tau_2$  lifetime may be a combination of intrinsic (triplet) and protein-induced (PET) photophysics.  
 224 Chain motions on the sub- $\mu\text{s}$  ( $\tau_1$ ) timescale are typically associated with interconversion of states  
 225 within the disordered conformational ensemble and with proximal loop formation.(40, 41) The  
 226 intermediate ( $\tau_2$ ) timescale is similar to that of forming transient secondary structure and distal  
 227 chain contacts (42), while the slowest ( $\tau_3$ ) kinetics is on the same timescale as concerted motions  
 228 of the protein chain, such as domain movements or transient tertiary structural contacts (43, 44).



229  
 230 **Figure 2.** FCS lifetimes of 4E-BP2 labelled with Atto488 at residue 0, 14, 35, 73, 91 or 121. Experimental  
 231 curves were fit to **Eq. 3**. NP 4E-BP2 labeled at residue 73 was fitted with 1, 2 or 3 kinetic decay components  
 232 (**A**), with the kinetic decays and diffusion for the best fit plotted separately (**B**). FCS experiments were  
 233 performed on 4E-BP2 in different states: non-phosphorylated (**C**), hyper-phosphorylated (**D**), in the  
 234 presence of  $0.5$   $\mu\text{M}$  of eIF4E (**E**), and in the presence of  $6$  M GdmCl (**F**). Different decay timescales are

235 shown in different colors:  $\tau_1=0.03-1 \mu\text{s}$  (red),  $\tau_2=3-30 \mu\text{s}$  (green) and  $\tau_3\approx 100 \mu\text{s}$  (blue). The fitting error  
 236 bars for each lifetime are shown in the figure. The full list of fitting parameters is given in **Table 2**.

237  
 238 For NP 4E-BP2, three kinetic components were resolved at each labelling position, which  
 239 follow the  $\tau_1$ ,  $\tau_2$  and  $\tau_3$  timescales. The lifetimes and amplitudes are highly site-dependent,  
 240 especially for the two fastest components (**Fig. 2C**). These results show higher flexibility in the  
 241 central region of the protein that folds upon phosphorylation, and in the C-terminal region, in  
 242 agreement with previous NMR data(12, 23). Similar PET-FCS analysis, with multiple lifetimes of  
 243 intrachain dynamics between  $\sim 100$  ns and  $\sim 100 \mu\text{s}$ , was previously reported for other IDPs, e.g.,  
 244 the N-terminal domain of p53-TAD (42) and the mouse prion protein moPrP (43).

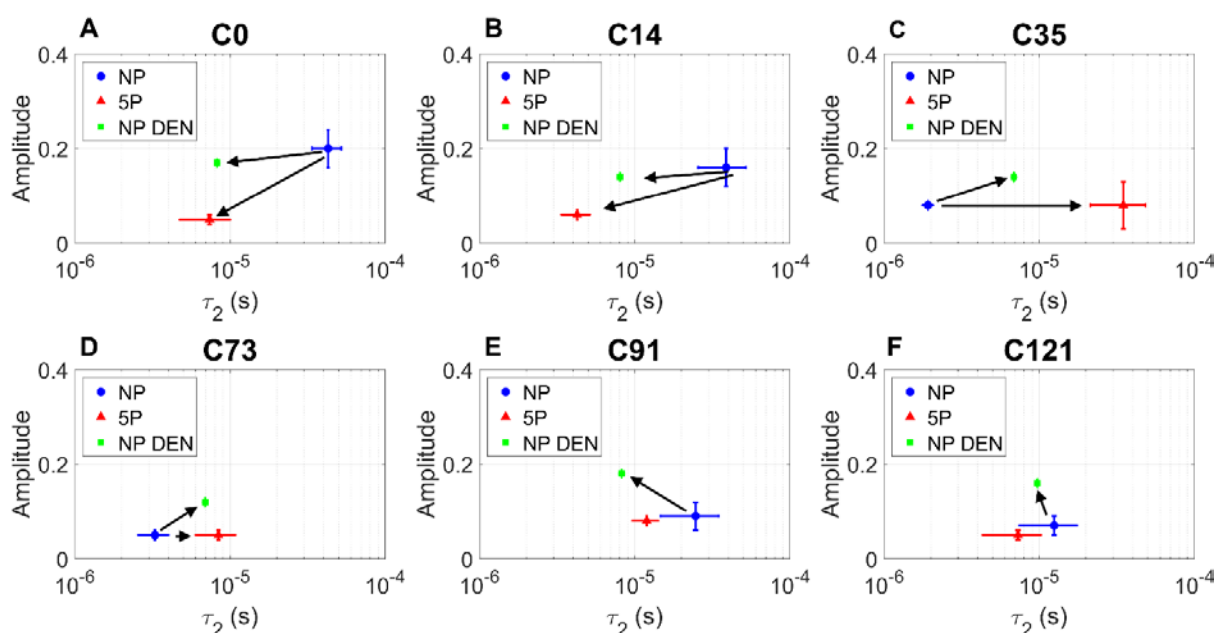
245  
 246 **Table 2.** FCS decay parameters for five-phospho, non-phospho and eIF4E-bound 4E-BP2 <sup>a</sup>.

	5P-BP2			NP-BP2			NP-BP2 + eIF4E		
	$\tau_1(\mu\text{s})$	$\tau_2(\mu\text{s})$	$\tau_3(\mu\text{s})$	$\tau_1(\mu\text{s})$	$\tau_2(\mu\text{s})$	$\tau_3(\mu\text{s})$	$\tau_1(\mu\text{s})$	$\tau_2(\mu\text{s})$	$\tau_3(\mu\text{s})$
<b>C0</b>	0.10 (0.17)	7.4 (0.05)	70.2 (0.02)	0.45 (0.06)	42.9 (0.20)	183.9 (0.21)	0.50 (0.07)	15.2 (0.10)	104.9 (0.24)
<b>S14C</b>	-	4.3 (0.06)	83.9 (0.24)	0.54 (0.07)	38.8 (0.16)	161.6 (0.22)	0.88 (0.08)	35.5 (0.11)	164.4 (0.26)
<b>C35</b>	-	34.8 (0.08)	110.9 (0.18)	0.09 (0.10)	1.9 (0.08)	61.4 (0.16)	0.10 (0.15)	7.9 (0.06)	91.8 (0.25)
<b>C73</b>	-	8.4 (0.05)	90.9 (0.22)	0.21 (0.07)	3.3 (0.05)	63.3 (0.16)	0.04 (0.36)	1.8 (0.04)	89.0 (0.24)
<b>S91C</b>	-	11.9 (0.08)	92.5 (0.19)	0.18 (0.08)	24.7 (0.09)	112.0 (0.25)	0.05 (0.28)	4.8 (0.08)	90.0 (0.24)
<b>C121</b>	-	7.3 (0.05)	76.1 (0.19)	0.02 (0.24)	12.5 (0.07)	95.7 (0.25)	0.49 (0.22)	7.8 (0.58)	68.4 (0.29)

247 <sup>a</sup> All data were fit to **Eq. 3** Lifetimes are given in microseconds, with corresponding amplitudes between brackets.  
 248 Fitting errors are given in SI (Table S3).

249  
 250 In contrast to the NP state, the 5P state exhibits only two FCS kinetic components ( $\tau_2$  and  
 251  $\tau_3$ ) at each labelling position, except for the C0 which required three (**Fig. 2B**). Likewise, the fast

252 ( $\tau_1$ ) kinetic component was not resolved in the chemically denatured state of 4E-BP2 (**Fig. 2D**).  
 253 Surprisingly, the 5P state and the denatured state show similar lifetimes along the sequence, with  
 254 the denatured state having a more uniform distribution than 5P. For both samples, the  $\tau_1$  kinetics  
 255 may have accelerated to timescales faster than 50 ns, such that it is not resolvable in our  
 256 measurements. This is likely the case for the denatured state, as for protein L the rate of  
 257 intramolecular contact is  $\sim 20$  times faster in 6 M GdmCl(45). However, for the 5P state, the  
 258 addition of phosphate groups and the induced folding in the 18-62 region probably slows down  
 259 the protein reconfiguration time sufficiently to be “absorbed” into the  $\tau_2$  kinetic component, as  
 260 previously reported for p53-TAD (42).  
 261



262  
 263 **Figure 3.** The changes in lifetime ( $\tau_2$ ) and amplitude ( $a_2$ ) of the intermediate FCS kinetic component  
 264 induced by multisite phosphorylation or by chemical denaturation (6 M GdmCl). 4E-BP2 was labelled with  
 265 Atto488 at positions 0, 14, 35, 73, 91 and 121 along the sequence, and the experimental FCS curves were  
 266 fit to **Eq. 3**. Different protein states are indicated as follows: non-phospho (**NP, blue circle**), five-phospho  
 267 (**5P, red triangle**), and non-phospho denatured (**NP DEN, green square**). The fitting error bars for each  
 268 parameter are indicated in the figure; all fitting parameters are given in **Table 2**.

269

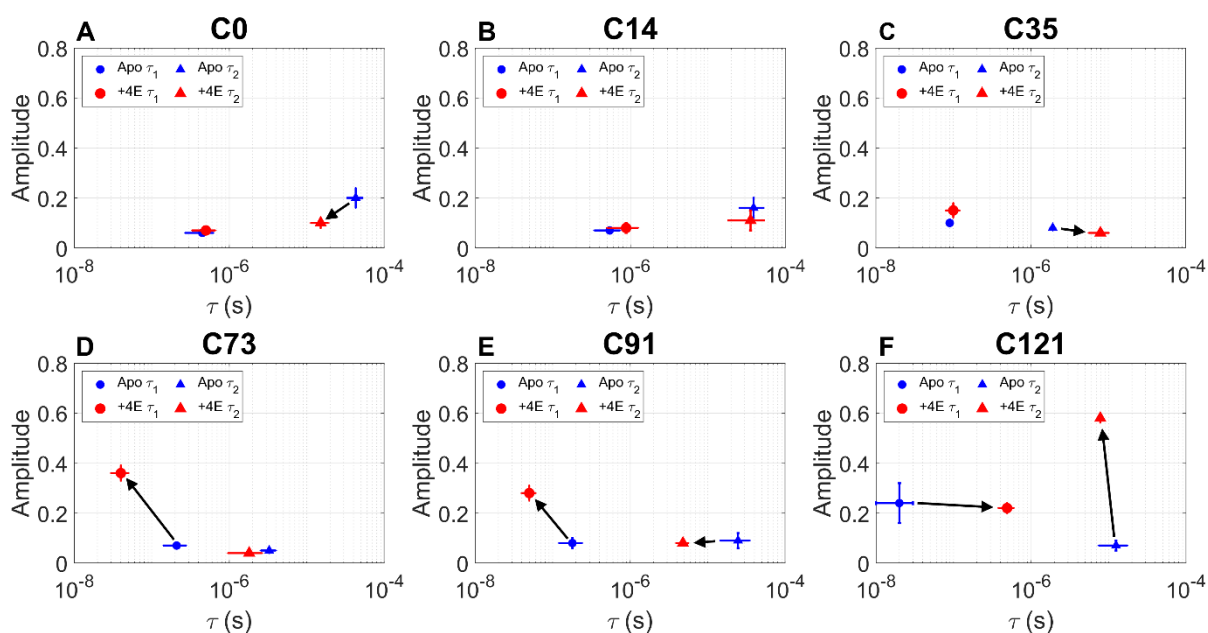
270 Upon phosphorylation, the  $\tau_2$  kinetics speeds up at positions 0, 14 and 91 and it slows down  
271 at positions 35 and 73; the associated kinetic amplitude  $a_2$  decreases at sites 0 and 14 and does not  
272 change at the other sites (**Fig. 3, Table 2**). Sites 35 and 73 are most proximal to the sites of  
273 phosphorylation (i.e., T37, T46, T70, S65 and S83), from which it can be inferred that the dominant  
274 effect of phosphorylation is to slow down intrachain contacts causing PET quenching. Similarly,  
275 slower conformational dynamics upon multisite phosphorylation has been observed for the  
276 disordered p53-TAD protein, even though phosphorylation does not lead to folding in this  
277 system.(42) In 4E-BP2, phosphorylation stabilizes the  $\beta$ -strand structure between residues 18 and  
278 62, which is expected to limit the access of the fluorophore to tyrosine quenchers.(12)

279 For the denatured state of NP 4E-BP2 (in 6 M GdmCl), only the  $\tau_2$  and  $\tau_3$  kinetic  
280 components were observed (**Fig. 2D**); nearly identical results were obtained for denatured 5P 4E-  
281 BP2 under the same GdmCl conditions (**Table S3**). The fitted lifetimes and their respective  
282 amplitudes showed little variance along the chain, e.g.,  $\tau_2 = 7\text{-}10 \mu\text{s}$  and  $\tau_3 = 100\text{-}120 \mu\text{s}$ . This  
283 highlights the influence that residual transient secondary and tertiary structure have on the  
284 conformational ensemble of disordered states and on the intrachain dynamics of 4E-BP2. The  
285 changes observed are consistent with denaturants (good solvents) reducing the strength of  
286 intramolecular interactions (hydrophobic, hydrogen bonds, van der Waals) in the context of  
287 protein-protein and protein-solvent interactions.<sup>5,9</sup>

288 Given the tight binding affinity of 4E-BP2 for eIF4E ( $k_d = 3.2 \pm 0.6 \text{ nM}$ )(12), saturating  
289 amounts of eIF4E ( $0.5 \mu\text{M}$ ) were used to ensure that nearly all (>99%) 4E-BP2 molecules were in  
290 the bound state. FCS measurements on Atto488-labelled 4E-BP2 w/wo unlabeled eIF4E (**Fig. S3**)  
291 showed a shift to longer diffusion times (larger  $R_H$ ) in the presence of eIF4E, which is consistent  
292 with the formation of the 4E-BP2:eIF4E complex. The  $R_H$  values estimated by fitting the data to

293 **Eq. 3** are  $29.0 \pm 0.5 \text{ \AA}$  for the NP 4E-BP2 (independent of labelling site) and  $36.6 \pm 0.8 \text{ \AA}$  for the  
 294 4E-BP2:eIF4E complex. As reference, FCS measurements of Atto488 (5 nM) in the presence of  
 295 excess eIF4E (1  $\mu\text{M}$ ) showed that the dye does not interact/bind with eIF4E (**Fig S3**).

296 When bound to eIF4E, NP 4E-BP2 exhibits three FCS kinetic components which fall into  
 297 the same  $\tau_1$ ,  $\tau_2$ , and  $\tau_3$  range as in the free (Apo) state. eIF4E (PDB: 3AM7) contains 8 Trp and 6  
 298 Tyr residues, of which four Trp (W46, W56, W73 and W102) and three Tyr (Y34, Y76, and Y  
 299 145) residues are largely surface exposed (**Table S4**). Therefore, the observed changes in PET  
 300 quenching dynamics are the combined result of the new inter-molecular interactions between 4E-  
 301 BP2 and the surface of eIF4E and the changes in intra-molecular contacts within 4E-BP2.



302 **Figure 4.** The changes in lifetime and amplitude of the two fastest FCS kinetic components ( $\tau_1$  – circle,  
 303 and  $\tau_2$  – triangle) induced by binding of NP 4E-BP2 to eIF4E. FCS measurements on NP 4E-BP2 labelled  
 304 with Atto488 at six different sites were performed in the Apo state (blue) and in the presence of 0.5  $\mu\text{M}$   
 305 eIF4E (red), and the data were fit to **Eq. 3**. The fitting error bars for each parameter are indicated in the  
 306 figure; all fitting parameters are given in **Table 2**.

308 4E-BP2 interacts with eIF4E through dynamic interactions involving at least an  $\alpha$ -helical  
 309 structure at the canonical  $^{54}\text{YXXXXL}\Phi^{60}$  motif and the secondary  $^{78}\text{IPGVT}^{82}$  site (20, 21).  
 310 Positions 73 and 91 show a decrease in lifetime accompanied by an increase in amplitude of the

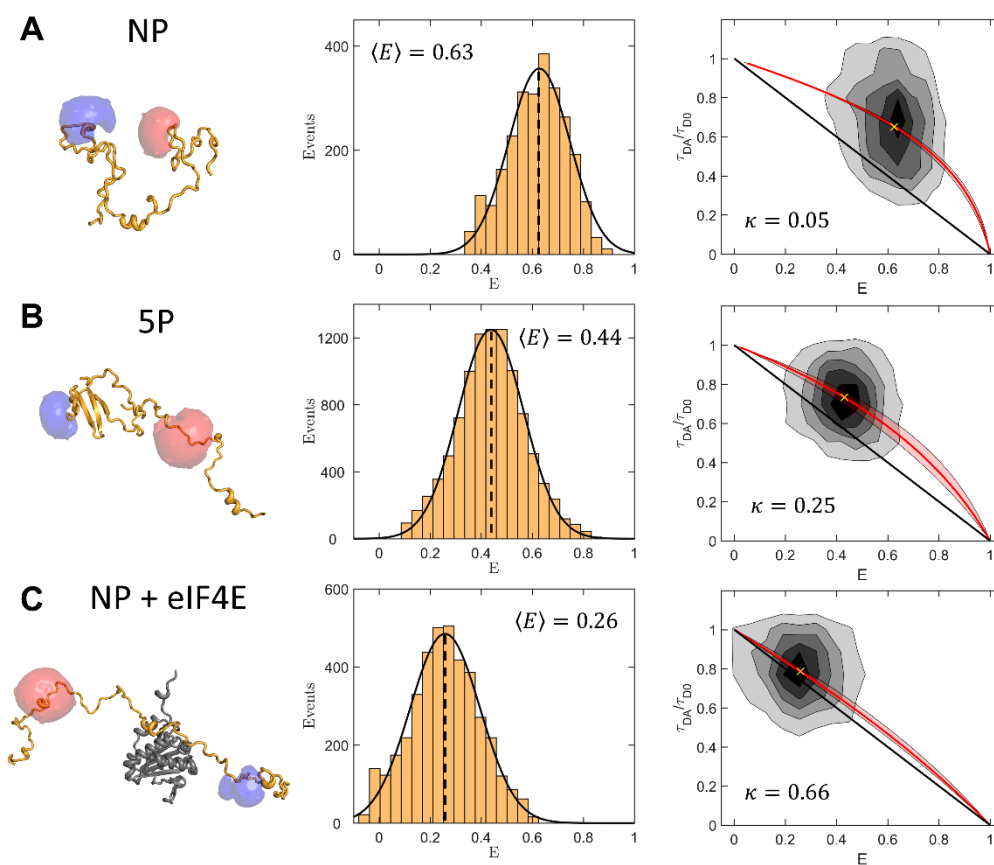
311 fast component, and a slight decrease in lifetime of the intermediate component upon binding to  
312 eIF4E (**Fig. 4 D-E**). As such,  $\tau_1$  decreases from ~200 ns to 40-50 ns upon binding, while the  
313 decrease in  $\tau_2$  is more prominent at position 91, i.e., from ~25  $\mu$ s to ~5  $\mu$ s (**Table 2**). The changes  
314 at the C-terminus are also significant, with increases of the  $\tau_1$  lifetime and of the amplitude of the  
315  $\tau_2$  component (**Fig. 4 F**). The decrease in lifetime and increase in amplitude of the  $\tau_2$  components  
316 of positions 73 and 91 are likely caused by dynamic exchange of the secondary binding site leading  
317 to quenching by aromatic residues on the surface of eIF4E. The involvement of residues 73, 91  
318 and 121 in eIF4E binding is consistent with binding-induced NMR intensity changes reported  
319 previously(20). The changes at residue 121 upon binding mirror those observed by FAD (**Fig. 1**  
320 **D**), providing further support for a dynamic complex involving more of the C-terminal portion of  
321 4E-BP2. Taken together, the results highlight the dynamic nature and range of timescales present  
322 in the bound state and ability of PET-FCS to probe intermolecular dynamics within the bound  
323 state.

### 324 **Chain dimensions and stiffness of 4E-BP2 assessed by smFRET**

325 smFRET is exquisitely suited to delineate heterogeneous and dynamic states that are  
326 inherent to IDPs. smFRET can resolve heterogeneous population distributions and kinetics, is  
327 compatible with a wide range of solution conditions, and overcomes the ensemble averaging of  
328 established structural techniques such as NMR and small-angle X-ray scattering (SAXS)(25). By  
329 recording the arrival time, the color and the polarization of each detected photon, multiparameter  
330 fluorescence (MPF) detection permits access to additional intrinsic properties of fluorescence that  
331 can be related to properties of the conjugated molecule (46). The chain dimensions and stiffness  
332 of 4E-BP2 were assessed using smFRET with MPF on two double-cysteine FRET constructs,  
333 which were labelled stochastically with Alexa Fluor 488 (donor) and Alexa Fluor 647 (acceptor).



334 smFRET histograms for H32C/S91C in the NP, 5P, and NP+eIF4E states are shown in **Fig.**  
 335 **5**. Although each histogram was satisfactorily fit to a single Gaussian, a single FRET peak does  
 336 not necessarily reflect a homogenous distribution of states. Indeed, the underlying population  
 337 could be in fast exchange compared to the burst duration ( $\sim 1$  ms). The data suggests that the NP  
 338 state is more compact than a statistical coil ensemble, i.e.,  $\langle E_{32-91}^{NP} \rangle_{exp} = 0.63 \pm 0.02$  vs.  
 339  $\langle E_{32-91}^{NP} \rangle_{coil} = 0.43 \pm 0.03$  (see SI section 2.3). This is consistent with the presence of transient  
 340 secondary structure observed by NMR(20), and with the multiple transient intrachain contacts  
 341 observed by PET-FCS.



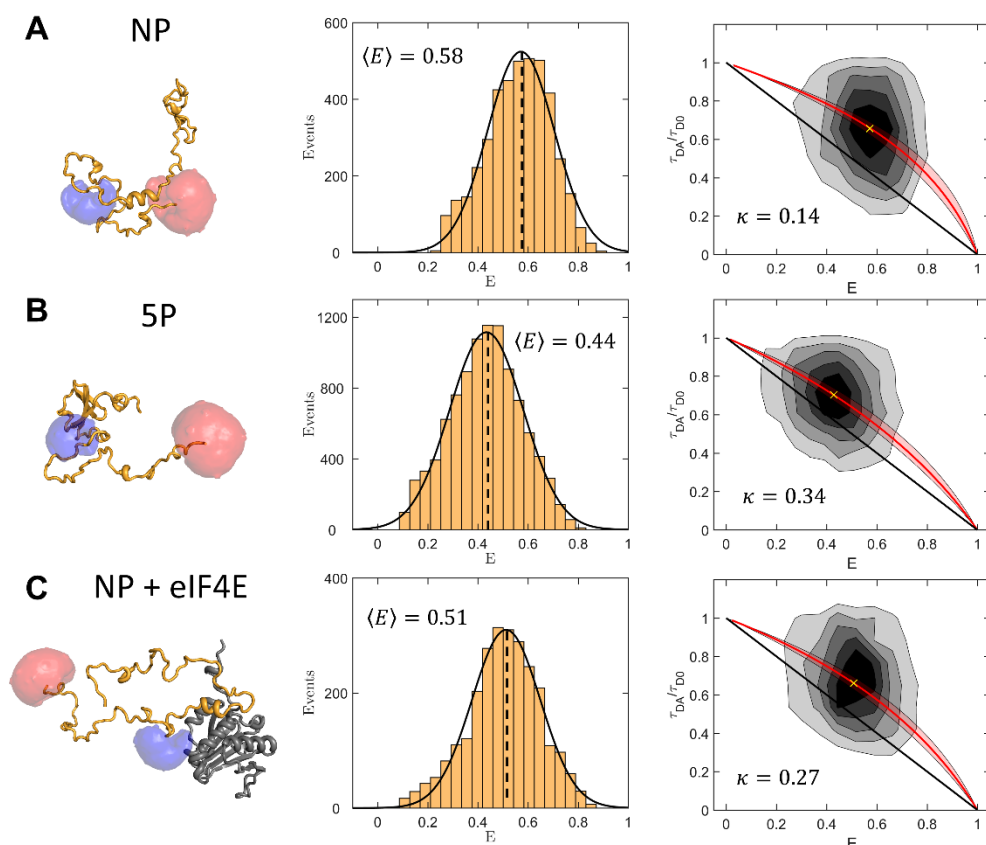
342  
 343 **Figure 5.** smFRET MPF results for the H32C/S91C 4E-BP2 construct labelled with Alexa Fluor 488 and  
 344 Alexa Fluor 647 in the (A) non-phospho (NP), (B) five-phospho and (5P) (C) non-phospho eIF4E-bound  
 345 (NP+eIF4E) states. (1<sup>st</sup> column) Cartoon depictions of conformations of 4E-BP2 in different states with  
 346 representations of fluorophore accessible volume simulations (47). (2<sup>nd</sup> column) FRET efficiency  
 347 histograms fit to a Gaussian function, with the dashed lines indicating the mean values. (3<sup>rd</sup> column) 2D  
 348 histogram plots of the FRET efficiency ( $E$ ) and the donor-only normalized fluorescence lifetime;  $\tau_{DA}$  and

349  $\tau_{D0}$  are donor lifetimes in the presence and absence of acceptor, respectively. The black line shows the  
350 relation expected for a static rigid molecule. The red line is a relation for a worm-like chain with a stiffness  
351 parameter ( $\kappa$ ) that passes through the centroid of a 2D gaussian fit indicated by a yellow cross. The red  
352 shaded region shows the uncertainty range of  $\kappa$ .

353  
354 Upon multi-site phosphorylation 4E-BP2 undergoes folding to a beta-sheet domain  
355 between residues 18 and 62 (12). Typically, when proteins fold, FRET efficiency increases,  
356 following the overall compaction of the structure and contraction of most (but not all!) inter-  
357 residue distances(48, 49). In this case however, the FRET efficiency of the 5P state is lower for  
358 the dye pairs at residues 32 and 91,  $\langle E_{32-91}^{5P} \rangle_{exp} = 0.44 \pm 0.02$ , not higher than the NP state,  
359  $\langle E_{32-91}^{NP} \rangle_{exp} = 0.63 \pm 0.02$  (**Table 3**). The dye at C32 is positioned in the long loop between  
360 strands  $\beta 1$  and  $\beta 2$  which is proximal to the C-terminal end of the domain (PBD ID 2MX4), from  
361 where the C-IDR, containing the dye at C91, extends. An alternate construct designed to  
362 specifically probe the folded region (with both dyes within the folded domain boundaries from 18-  
363 62) would likely lead to an increase in FRET efficiency upon phosphorylation. The H32C/S91C  
364 construct, however, also partially probes the C-IDR, which expands when 4E-BP2 is  
365 phosphorylated (**Fig. 5B**).

366 The FRET efficiency of the NP H32C/S91C construct exhibits an even larger decrease  
367 upon binding to eIF4E, i.e.,  $E_{32-91}^{NP+4E} = 0.26 \pm 0.02$ . This construct flanks both primary and  
368 secondary binding sites and should be sensitive to 4E-BP2:eIF4E interactions and the 3D  
369 arrangement of the complex. The large FRET decrease could result from a combination of more  
370 extended conformations being compatible with the eIF4E bound state, in which 4E-BP2 wraps  
371 around eIF4E (with the exception of the canonical helical element), and an excluded-volume effect  
372 exerted by eIF4E on 4E-BP2. The conformations of 4E-BP2 bound to eIF4E are thought to be  
373 defined by dynamic interactions of the canonical and secondary binding elements, and by  
374 significant structural disorder elsewhere (20).

375 smFRET histograms of the C73/C121 construct for the same three 4E-BP2 states are shown  
376 in **Fig. 6**. The average FRET efficiency for NP 4E-BP2,  $\langle E_{73-121}^{NP} \rangle_{exp} = 0.58 \pm 0.02$ , is also  
377 higher than that expected from a statistical coil,  $\langle E_{73-121}^{NP} \rangle_{coil} = 0.49 \pm 0.03$ , suggesting that the  
378 C-terminal disordered region contains transient intrachain contacts. The average C73/C121 FRET  
379 efficiency decreases to  $\langle E_{73-121}^{5P} \rangle = 0.44 \pm 0.02$  upon phosphorylation, but only to  $\langle E_{73-121}^{NP+4E} \rangle =$   
380  $0.51 \pm 0.02$  upon binding to eIF4E. The electrostatic repulsion between the five phosphates may  
381 contribute to the C-IDR expansion of 5P 4E-BP2. This expansion of the C-IDR has also been  
382 observed from previously published NMR paramagnetic relaxation enhancement (PRE) data and  
383 chemical shift-derived measures of secondary structure.(23)



384  
385 **Figure 6.** smFRET MPF results for the C73/C121 4E-BP2 construct labelled with Alexa Fluor 488 and  
386 Alexa Fluor 647 in the (A) non-phospho (NP), (B) five-phospho (5P) and (C) non-phospho eIF4E bound  
387 states (NP+4E). (1<sup>st</sup> column) Cartoon depictions of conformations of 4E-BP2 in different states with  
388 representations of fluorophore accessible volume simulations (47). (2<sup>nd</sup> column) FRET efficiency

389 histograms fit to a Gaussian function, with the dashed lines indicating the mean values. (3<sup>rd</sup> column) 2D  
 390 histograms plots of the FRET efficiency ( $E$ ) and the donor-only normalized fluorescence lifetime;  $\tau_{DA}$  and  
 391  $\tau_{D0}$  are donor lifetimes in the presence and absence of acceptor, respectively. The black line shows the  
 392 relation expected for a static rigid molecule. The red line is a relation for a worm-like chain with a stiffness  
 393 parameter ( $\kappa$ ) that passes through the centroid of a 2D gaussian fit indicated by a yellow cross. The red  
 394 shaded region shows the uncertainty range of  $\kappa$ .

395  
 396 For the bound state, the reduction in FRET is much less for C73/C121 than for H32C/S91C, i.e.,

397  $\Delta E_{73-121}^{NP \rightarrow +4E} = -(0.07 \pm 0.03)$  vs.  $\Delta E_{32-91}^{NP \rightarrow +4E} = -(0.37 \pm 0.03)$ . This suggests that C-terminal

398 disordered conformations are less restricted in the 4E-BP2:eIF4E complex than those of the 32-91

399 region, as expected from the complete loss or very significant broadening of NMR resonances

400 upon binding from residues 34-90 (20).

401 The relation between the donor lifetime and the FRET efficiency can be used to infer  
 402 information about the dynamic exchange of the underlying states (50). A linear relation is expected  
 403 for a static structure, with conformations that are rigid or fluctuate on a timescale slower than  $\sim 100$   
 404  $\mu\text{s}$ ; in contrast, a nonlinear relation is expected for IDPs, as inter-photon times (1-10  $\mu\text{s}$ ) are much  
 405 larger than typical chain reconfiguration times ( $\sim 100$  ns) (51). A family of dynamic  $\tau$  vs.  $E$  lines  
 406 based on a worm-like chain (WLC) model with variable stiffness  $\kappa$  (or persistence length) was  
 407 generated using a method described by Barth et al. (52) The center of the experimental 2D FRET  
 408 histogram was best matched to a WLC curve to infer the average stiffness for different regions of  
 409 4E-BP2 in different phospho/binding states (**Table 3**).

410 **Table 3.** Mean smFRET efficiency and WLC stiffness values of the non-phospho (NP), five-phospho  
 411 (5P) and eIF4E-bound 4E-BP2 (NP+4E).

	NP-BP2		5P-BP2		NP-BP2 + eIF4E	
	$\langle E \rangle$	$\kappa$	$\langle E \rangle$	$\kappa$	$\langle E \rangle$	$\kappa$
<b>H32C/ S91C</b>	$0.63 \pm 0.02$	$0.05 \pm 0.03$	$0.44 \pm 0.02$	$0.25 \pm 0.10$	$0.26 \pm 0.02$	$0.66 \pm 0.17$
<b>C73/ C121</b>	$0.58 \pm 0.02$	$0.14 \pm 0.08$	$0.44 \pm 0.02$	$0.34 \pm 0.10$	$0.51 \pm 0.02$	$0.27 \pm 0.08$

412 The stiffness parameter of the 32-91 region,  $\kappa_{32-91}^{NP} = 0.05 \pm 0.03$ , corresponds to a  
413 persistence length of  $l_p^{NP} = 1.0 \pm 0.6$  nm, which is similar to  $l_p = 0.4 \pm 0.07$  nm reported for  
414 a set of disordered and unfolded proteins.(53) The stiffness increases to  $\kappa_{32-91}^{5P} = 0.25 \pm 0.10$   
415 upon phosphorylation, and even more significantly, to  $\kappa_{32-91}^{NP+4E} = 0.66 \pm 0.17$  upon binding to  
416 eIF4E (**Fig. 5** and **Table 3**). The larger stiffness in the 5P state is consistent with the appearance  
417 of a stable beta-fold between residues 18 and 62. In the bound state, the 2D FRET population lies  
418 close to the static line; this is consistent with the decreased dynamics expected as residues 49-67  
419 form a predominantly stable helix when 4E-BP2 is bound to eIF4E.(20, 54) At the same time, the  
420 separation between the static and dynamic regimes is much reduced in the low  $E$  range, which  
421 increases the uncertainty in estimating the chain stiffness.

422 The 73-121 region has a stiffness of  $\kappa_{73-121}^{NP} = 0.14 \pm 0.08$  and  $\kappa_{73-121}^{5P} = 0.34 \pm 0.10$   
423 in the NP and 5P states, respectively. While slightly larger, these values mirror the changes  
424 observed for the 32-91 region. The stiffening of the C-IDR upon phosphorylation can be attributed  
425 to stabilizing interactions with the folded domain established previously (23). However, in contrast  
426 to the 32-91 region, the stiffness of the C-terminal region shows only a moderate increase in the  
427 eIF4E-bound state, to  $\kappa_{73-121}^{NP+4E} = 0.27 \pm 0.08$ , as the 2D FRET histogram remains well separated  
428 from the static line (**Fig. 6**). Together with the FAD and PET-FCS results, this suggests that the  
429 73-121 region remains disordered and interacts with eIF4E as part of a more extensive dynamic  
430 complex than the current bipartite model (20).

431

## 432 CONCLUSIONS

433 Dynamics is likely the key factor in understanding how 4E-BP2 regulates cap-dependent  
434 translation via interactions with the initiation factor eIF4E. Complementary to our previous NMR

435 studies of the 4E-BP2 protein (12, 20, 23), a suite of multiparameter fluorescence techniques was  
436 used here to define local and global conformational dynamics of this intriguing IDP in its various  
437 states. Polarization anisotropy (FAD) measurements showed evidence of heterogeneous chain  
438 flexibility within the 4E-BP2 sequence, which correlates with variations in transient secondary  
439 structure and local amino acid composition. Multisite phosphorylation decreased segmental  
440 flexibility only in the region that undergoes folding (residues 18-62), while it made the rest of the  
441 chain more flexible. As anticipated, in the presence of eIF4E, segmental dynamics near the two  
442 binding sites was slowed down by binding interactions. Surprisingly however, the C-terminal  
443 region adjacent to the secondary binding site experienced the largest changes, while the N-terminal  
444 region exhibited much less change. These results implicate a much larger region of 4E-BP2  
445 interacting with eIF4E than previously thought, and showcase FAD as a sensitive method to probe  
446 local binding affinity, at the level of individual protein segments, in the context of multivalent  
447 interactions.

448       As seen previously for other IDPs (42), the quenching rates decreased at labelling sites  
449 closest to the phosphorylation sites and within the folded domain, and increased at the other sites.  
450 This likely arises from a combination of local steric and electrostatic effects of the phosphate  
451 groups and the overall steric effect of the folded domain. In the presence of eIF4E, the quenching  
452 rates near the two binding motifs in 4E-BP2 increased significantly, as expected from increased  
453 contacts with several exposed Trp and Tyr residues along the extensive binding interface of eIF4E.  
454 Although contributions from intra- and inter-molecular contact could not be distinguished, the  
455 significant changes observed at the C-terminus support the involvement of the C-terminal region  
456 of 4E-BP2 in dynamic interactions with eIF4E.

457 smFRET measurements informed on changes in 4E-BP2 chain dimensions and stiffness of  
458 central and C-terminal regions of the protein following phosphorylation or binding. In the NP state,  
459 as a consequence of transient intrachain secondary and tertiary contacts, the donor-acceptor  
460 distance turned out smaller (higher FRET efficiency) than the random coil prediction for both  
461 FRET constructs. In the 5P state, the separation between residues 32 and 91, which partially  
462 contains the folding domain, increased, instead of the decrease typically expected for a folding  
463 transition. When bound to eIF4E, the chain expands and stiffens considerably around the canonical  
464 and secondary binding sites, while the C-terminal region remains highly flexible. The canonical  
465 binding motif and secondary binding site provide specificity, while the dynamic nature of the  
466 complex which retains significant chain flexibility minimizes the entropic penalty. All  
467 phosphorylation sites except S65, which is phosphorylated last, are in regions that remain highly  
468 dynamic in the 4E-BP2:eIF4E complex. This facilitates the access of large kinases and allows a  
469 rapid response to cellular conditions. Our fluorescence-based characterization of the 4E-BP2  
470 conformational dynamics is an important step towards understanding the interplay between folding  
471 and release of binding to eIF4E and its regulatory function, and it provides a foundation for future  
472 studies of IDP conformational and binding equilibria.

## 473 MATERIALS AND METHODS

474 **Materials.** The fluorescent probes used for labelling the 4E-BP2 protein for SMF  
475 experiments were: Alexa 488 (A488) maleimide, Alexa 647 (A647) maleimide (ThermoFisher  
476 Scientific, Canada) and Atto 488 (At488) maleimide (ATTO-TEC GmbH, Germany).  
477 Guanidinium chloride (GdmCl) (G9284, Sigma Aldrich) was used for protein denaturation. All  
478 samples were diluted in phosphate-buffered saline (PBS) containing 137 mM NaCl, 2.7 mM KCl,  
479 10 mM Na<sub>2</sub>HPO<sub>4</sub>, and 1.8 mM KH<sub>2</sub>PO<sub>4</sub> at pH 7.4. GdmCl solutions were adjusted to pH 7.4 for  
480 all the denaturation experiments.

481 **Protein expression and purification.** Small ubiquitin-like modifier (Sumo) fusion  
482 constructs of both the 4E-BP2 protein (residues 1 through 120) and eIF4E protein (residues 1  
483 through 217) were expressed and purified as described previously(23). Briefly, the proteins were  
484 expressed in BL21-codonplus (DE3)-RIPL competent *E. coli* cells (Agilent Technologies) in  
485 Lysogeny broth at 37 °C until OD<sub>600</sub>~0.6-0.8, induced with isopropyl β-D-1-thiogalactopyranoside  
486 (IPTG), and expressed at 16 °C for ~16 h. Protein was purified from cell lysate with a nickel–  
487 nitrilotriacetic acid (Ni–NTA) column followed by cleavage of the Sumo solubility tag with ULP1  
488 at 4 °C for ~16 h. The Sumo tag was separated using an N-NTA column followed by HiLoad  
489 Superdex 75 PG gel filtration column (28-9893-34, GE Healthcare) if the protein was not pure as  
490 assessed by SDS-PAGE. The molecular mass and the purity of protein samples were verified by  
491 electrospray ionization mass spectrometry (ESI-MS).

492 Phosphorylation of 4E-BP2 with activated Erk2 using a dialysis technique was performed  
493 as described previously(12, 23). Briefly, 50 mL of 5 μM Erk2 and 20 μM of 4E-BP2 were dialyzed  
494 in a 3 kDa MWCO dialysis bag in 1 L of buffer. The dialysis buffer contained 50 mM Tris-HCl,  
495 pH 7.5, 1 mM EGTA, 5 mM BME, 20 mM MgCl<sub>2</sub>, and 10 mM EDTA, dialysis was performed at



496 20 °C for 1-3 days. Phosphorylated 4E-BP2 was purified from Erk2 using a Ni-NTA column.  
497 Purity and degree of phosphorylation of 4E-BP2 was confirmed by ESI-MS.

498 All single cysteine proteins (C0/C35S/C73S (cysteine insertion at 0 position),  
499 S14C/C35S/C73S, C35/C73S, C73/C35S, C35S/C73S/S91C, C35S/C73S/C121 (insertion at 121  
500 position)) were labeled by adding the At488 maleimide fluorophore to a 50 µL solution of 100 µM  
501 protein at a dye:protein molar ratio of 3:1. The double-cysteine mutants (H32C/C35S/C73S/S91C)  
502 and (C35S/insC121) was labeled with A488 maleimide and A647 maleimide by adding A488 and  
503 A647 to a 50 µL solution of 100 µM protein at a A488:A647:protein molar ratio of 1.3:3:1. TCEP  
504 was added at a 10× molar excess to the protein in order to reduce the disulfide bonds. All the  
505 maleimide-cysteine coupling reactions were performed in a PBS buffer at pH 7.4. Oxygen was  
506 removed by flushing the sample with argon gas in a desiccator for 5 min. The vial was capped  
507 tightly and shaken gently for 3 hours at room temperature. The excess dye was removed by size-  
508 exclusion chromatography using Sephadex G-50 gels (G5080, Sigma Aldrich) in a BioLogic LP  
509 system (731-8300, Bio-Rad).

510 All samples were diluted to concentrations of 1–10 nM and 20–50 pM, which are most  
511 suitable for FCS/FAD and smFRET burst experiments, respectively. For a typical experiment, a  
512 sample solution of 30 µL was dropped on the surface of plasma-cleaned coverslip. Non-specific  
513 protein adsorption to the coverslip was prevented by adding 0.005% (v/v) Tween-20 (P2287,  
514 Sigma-Aldrich) to the solution, and bovine serum albumin (BSA) (15260-037, ThermoFisher  
515 Scientific) was used to coat the clean coverslips. All experiments were performed at 20 °C.

516 **Instrumentation.** smFRET measurements were performed on a custom-built  
517 multiparameter fluorescence microscope (32). The donor was excited at 480 nm by frequency

518 doubling the infrared output of a femtosecond laser (Tsunami HP, Spectra Physics), while the  
519 acceptor was excited at 635-nm using a diode laser (WSTech, TECRL-25GC-635). Alternating-  
520 laser excitation (ALEX) of the sample was performed by synchronous modulation of the two laser  
521 sources to achieve alternating 50- $\mu$ s periods of donor and acceptor fluorophore excitation,  
522 respectively. Laser intensities of 10 kW/cm<sup>2</sup> and 3.6 kW/cm<sup>2</sup> at the sample were used for exciting  
523 the donor and the acceptor fluorophores, respectively. FAD measurements were performed on the  
524 same microscope, by exciting Atto488 at an average intensity of  $\sim$ 0.14 kW/cm<sup>2</sup> at the sample. FCS  
525 measurements were performed on a separate custom-built fluorescence microscope described  
526 elsewhere (55), where Atto488 was excited using a 488-nm diode laser (TECBL-488nm,  
527 WorldStarTech) with a power of  $\sim$ 5  $\mu$ W at the sample.

528 **FAD analysis.** FAD monitors the rotation dynamics of the emission dipole of the dye. The  
529 “wobble-in-a-cone” model (30) was used to fit the experimental FAD data:

$$530 \quad r(t) = r_0[(1 - a)e^{-t/\rho_{dye}} + a]e^{-t/\rho_{seg}} + r_{inf} \quad (1)$$

531 where  $\rho_{dye}$ ,  $\rho_{seg}$  are rotational correlation lifetimes of the dye and the protein segment,  
532 respectively, and  $a$  is the fraction of the slower (segmental) component. The uncertainties of the  
533 fitted parameters were estimated by taking the standard deviation of the fitting results of 3-7 data  
534 sets collected consecutively; if any of the fitting derived errors were larger, then this value was  
535 reported. The baseline offset  $r_{inf}$  accounts for the slow, global motion of the whole protein; this  
536 is typically very small for IDPs due to their high backbone flexibility (29), but it can increase upon  
537 binding to their targets. The half-cone angle  $\theta$  describes the wobbling cone of the dye emission  
538 dipole (56):

$$539 \quad a = \left[ \frac{1}{2}(1 + \cos\theta)\cos\theta \right]^2 \quad (2)$$

540 **FCS analysis.** In FCS, the fluorescence autocorrelation function for free Brownian  
541 diffusion of a single molecular species with multiple relaxation components is given by (57) :

$$542 \quad G(\tau) = \frac{1}{N_{eff}} \left(1 + \frac{\tau}{\tau_d}\right)^{-1} \left(1 + \frac{\tau}{s^2\tau_d}\right)^{-0.5} \sum_i \left(1 + a_i e^{-\frac{\tau}{t_i}}\right) \quad (3)$$

543 In equation (3),  $N_{eff}$  is the average number of molecules in the detection volume,  $s$  is the  
544 ratio between the axial and the lateral radii of the detection volume ( $s = z_0/w_0$ ), and  $\tau_d$  is the  
545 average diffusion time, which is related to the diffusion coefficient ( $w_0^2 = 4D\tau_d$ ) and to the  
546 hydrodynamic radius  $R_H$  of the molecule via the Stokes-Einstein equation(58);  $a_i$  and  $t_i$  are the  
547 amplitude and the lifetime of the  $i^{\text{th}}$  relaxation component, respectively. Fitting was optimized by  
548 varying the number of relaxation components, the goodness of fit ( $\chi^2$ ) and Akaike information  
549 criterion (AIC) were calculated for each fit. The addition of relaxation component was accepted  
550 if: the  $\chi^2$  parameter decreased, the AIC decreased, and the fitting residuals were featureless. The  
551 uncertainties of the fitted parameters were estimated using the Jacobian from Levenberg-  
552 Marquardt least-squares fitting. Prior to each set of measurements, a calibration dye (rhodamine  
553 110) was used to estimate the  $s$  and  $w_0$  parameters, typically  $\sim 8$  and  $\sim 250$  nm, respectively.

554 **smFRET analysis.** A custom MATLAB script based on the ‘MLT’ algorithm was used to  
555 identify fluorescence bursts and sort them into donor-only, acceptor-only and dual-labelled  
556 (FRET) populations (32). The FRET efficiency for each burst was calculated based on the number  
557 of detected photons in the donor ( $I_D$ ) and acceptor ( $I_A$ ) channels:

$$558 \quad E = \frac{I_A}{I_A + \gamma I_D} \quad (4)$$

559 where  $\gamma$  (**Eq. 5**) is a correction factor for the difference in detection efficiencies of donor and  
560 acceptor channels ( $\eta_D$  and  $\eta_A$ ) and quantum yields of the dyes(46) ( $\Phi_D$  and  $\Phi_A$ ), and was  
561 determined as described previously(32):

$$562 \quad \gamma = \frac{\eta_A \Phi_A}{\eta_D \Phi_D} \quad (5)$$

563 In addition, corrections were applied on both  $I_D$  and  $I_A$  to subtract background, spectral cross talk,  
564 and direct excitation of the acceptor. The background was obtained from a measurement of the  
565 sample buffer while the corrections for cross talk and direct excitation were derived from donor-  
566 only and acceptor-only bursts. A smFRET histogram was constructed from all bursts detected for  
567 a given sample, each histogram was fit to a single Gaussian distribution.

568 To estimate the FRET efficiency if 4E-BP2 was a featureless statistical coil, 5000  
569 conformers were generated using Trajectory Directed Ensemble Sampling (TraDES)(59) with  
570 100% coil sampling in accordance with the sequences in **Table S1**. The FRET efficiency for each  
571 conformer was calculated using the python library *LabelLib*(60) (see SI section **2.3**).

572 For each FRET construct, a family of  $\tau_{DA}/\tau$  vs  $E$  curves were generated based on a WLC  
573 model with stiffness parameters  $\kappa$  between 0.01 and 1 using the *FRETlines* Python library(52).  
574 The chain stiffness for given dataset was selected as the  $\kappa$  value of the  $\tau_{DA}/\tau$  vs  $E$  curve passing  
575 through the centroid of a 2D Gaussian fit of the experimental  $\tau_{DA}/\tau$  vs  $E$  histogram. The confidence  
576 interval was established from the range of WLC models that agree with the centroid from fitting  
577 within the experimental accuracy of determining the FRET efficiency, i.e., 0.02 (32).

578

579

580 **AUTHOR INFORMATION**

581 **Corresponding Authors**

582 Email: [claudiu.gradinaru@utoronto.ca](mailto:claudiu.gradinaru@utoronto.ca)

583

584 **Author Contributions**

585 C.C.G. was responsible for overall project management and supervision. S.S. and Z.Z. expressed,  
586 purified and labelled proteins, performed measurements and analyzed data. A.B. and J.D. designed  
587 single- and double-cysteine 4E-BP2 mutants. T.T. performed smFRET simulations. S.S., Z.Z., and  
588 C.C.G. wrote the manuscript. J.D.F.-K. contributed to interpretation of results and critical revision  
589 of manuscript.

590

591 **Competing Financial Interest**

592 The authors report no competing financial interest.

593

594 **ACKNOWLEDGEMENTS**

595 This work has been supported by the Natural Sciences and Engineering Research Council of  
596 Canada (NSERC RGPIN 2017 – 06030 to C.C.G.), the Canadian Institutes of Health Research  
597 (CIHR FND-148375 to J.D.F.-K.) and National Institutes of Health (NIH 5R01GM127627-03 to  
598 J.D.F.-K.).

## 599 REFERENCES

- 600 1. P. E. Wright, H. J. Dyson, Intrinsically unstructured proteins: Re-assessing the protein structure-  
601 function paradigm. *Journal of Molecular Biology* **293**, 321-331 (1999).
- 602 2. V. N. Uversky, Intrinsically disordered proteins from A to Z. *The International Journal of*  
603 *Biochemistry & Cell Biology* **43**, 1090-1103 (2011).
- 604 3. P. E. Wright, H. J. Dyson, Intrinsically disordered proteins in cellular signalling and regulation.  
605 *Nature Reviews Molecular Cell Biology* **16**, 18-29 (2015).
- 606 4. C. Haynes *et al.*, Intrinsic disorder is a common feature of hub proteins from four eukaryotic  
607 interactomes. *PLoS Comput Biol* **2**, e100 (2006).
- 608 5. A. K. Dunker, I. Silman, V. N. Uversky, J. L. Sussman, Function and structure of inherently  
609 disordered proteins. *Current Opinion in Structural Biology* **18**, 756-764 (2008).
- 610 6. Julie D. Forman-Kay, T. Mittag, From Sequence and Forces to Structure, Function, and Evolution  
611 of Intrinsically Disordered Proteins. *Structure* **21**, 1492-1499 (2013).
- 612 7. V. N. Uversky, Natively unfolded proteins: A point where biology waits for physics. *Protein*  
613 *Science* **11**, 739-756 (2002).
- 614 8. J. A. Marsh, J. D. Forman-Kay, Sequence determinants of compaction in intrinsically disordered  
615 proteins. *Biophysical journal* **98**, 2383-2390 (2010).
- 616 9. A. H. Mao, S. L. Crick, A. Vitalis, C. L. Chicoine, R. V. Pappu, Net charge per residue modulates  
617 conformational ensembles of intrinsically disordered proteins. *Proceedings of the National*  
618 *Academy of Sciences* **107**, 8183-8188 (2010).
- 619 10. N. Sonenberg, A. G. Hinnebusch, Regulation of translation initiation in eukaryotes: mechanisms  
620 and biological targets. *Cell* **136**, 731-745 (2009).
- 621 11. S. Tait *et al.*, Local control of a disorder–order transition in 4E-BP1 underpins regulation of  
622 translation via eIF4E. *Proceedings of the National Academy of Sciences* **107**, 17627-17632 (2010).
- 623 12. A. Bah *et al.*, Folding of an intrinsically disordered protein by phosphorylation as a regulatory  
624 switch. *Nature* **519**, 106-109 (2015).
- 625 13. A. Lazaris-Karatzas, N. Sonenberg, The mRNA 5'cap-binding protein, eIF-4E, cooperates with v-  
626 myc or E1A in the transformation of primary rodent fibroblasts. *Molecular and cellular biology*  
627 **12**, 1234-1238 (1992).
- 628 14. A. Lazaris-Karatzas *et al.*, Ras mediates translation initiation factor 4E-induced malignant  
629 transformation. *Genes & development* **6**, 1631-1642 (1992).
- 630 15. A.-C. Gingras *et al.*, Regulation of 4E-BP1 phosphorylation: a novel two-step mechanism. *Genes*  
631 *& development* **13**, 1422-1437 (1999).
- 632 16. R. J. Dowling *et al.*, mTORC1-mediated cell proliferation, but not cell growth, controlled by the  
633 4E-BPs. *Science* **328**, 1172-1176 (2010).
- 634 17. R. Colina *et al.*, Translational control of the innate immune response through IRF-7. *Nature* **452**,  
635 323-328 (2008).
- 636 18. C. G. Gkogkas *et al.*, Autism-related deficits via dysregulated eIF4E-dependent translational  
637 control. *Nature* **493**, 371-377 (2013).
- 638 19. E. Klann, J. D. Sweatt, Altered protein synthesis is a trigger for long-term memory formation.  
639 *Neurobiology of learning and memory* **89**, 247-259 (2008).
- 640 20. S. Lukhele, A. Bah, H. Lin, N. Sonenberg, J. D. Forman-Kay, Interaction of the eukaryotic  
641 initiation factor 4E with 4E-BP2 at a dynamic bipartite interface. *Structure* **21**, 2186-2196 (2013).
- 642 21. D. Peter *et al.*, Molecular Architecture of 4E-BP Translational Inhibitors Bound to eIF4E.  
643 *Molecular Cell* **57**, 1074-1087 (2015).
- 644 22. G. J. Brunn *et al.*, Phosphorylation of the translational repressor PHAS-I by the mammalian target  
645 of rapamycin. *Science* **277**, 99-101 (1997).
- 646 23. J. E. Dawson *et al.*, Non-cooperative 4E-BP2 folding with exchange between eIF4E-binding and  
647 binding-incompatible states tunes cap-dependent translation inhibition. *Nat Commun* **11**, 3146  
648 (2020).

- 649 24. G.-N. Gomes, C. C. Gradinaru, Insights into the conformations and dynamics of intrinsically  
650 disordered proteins using single-molecule fluorescence. *Biochimica et Biophysica Acta (BBA) -*  
651 *Proteins and Proteomics* **1865**, 1696-1706 (2017).
- 652 25. L. A. Metskas, E. Rhoades, Single-molecule FRET of intrinsically disordered proteins. *Annual*  
653 *review of physical chemistry* **71**, 391-414 (2020).
- 654 26. V. N. Uversky, "Biophysical Methods to Investigate Intrinsically Disordered Proteins: Avoiding  
655 an "Elephant and Blind Men" Situation" in *Intrinsically Disordered Proteins Studied by NMR*  
656 *Spectroscopy*. (Springer, 2015), pp. 215-260.
- 657 27. G. F. Schröder, U. Alexiev, H. Grubmüller, Simulation of fluorescence anisotropy experiments:  
658 probing protein dynamics. *Biophysical journal* **89**, 3757-3770 (2005).
- 659 28. S. Milles, E. A. Lemke, Mapping Multivalency and Differential Affinities within Large  
660 Intrinsically Disordered Protein Complexes with Segmental Motion Analysis. *Angewandte Chemie*  
661 *International Edition* **53**, 7364-7367 (2014).
- 662 29. N. Jain, M. Bhattacharya, S. Mukhopadhyay, Chain collapse of an amyloidogenic intrinsically  
663 disordered protein. *Biophysical journal* **101**, 1720-1729 (2011).
- 664 30. J. R. Lakowicz, *Principles of fluorescence spectroscopy* (Springer, New York, N.Y., ed. 3rd, 2006).
- 665 31. Z. Zhang, D. Yomo, C. Gradinaru, Choosing the right fluorophore for single-molecule fluorescence  
666 studies in a lipid environment. *Biochimica et Biophysica Acta (BBA) - Biomembranes* **1859**, 1242-  
667 1253 (2017).
- 668 32. G.-N. W. Gomes *et al.*, Conformational Ensembles of an Intrinsically Disordered Protein  
669 Consistent with NMR, SAXS, and Single-Molecule FRET. *Journal of the American Chemical*  
670 *Society* **142**, 15697-15710 (2020).
- 671 33. F. Huang, W. M. Nau, A conformational flexibility scale for amino acids in peptides. *Angewandte*  
672 *Chemie* **115**, 2371-2374 (2003).
- 673 34. Keum *et al.*, A conserved motif within the flexible C-terminus of the translational regulator 4E-BP  
674 is required for tight binding to the mRNA cap-binding protein eIF4E. *Biochemical Journal* **441**,  
675 237-245 (2012).
- 676 35. A. P. De Silva, T. S. Moody, G. D. Wright, Fluorescent PET (Photoinduced Electron Transfer)  
677 sensors as potent analytical tools. *Analyst* **134**, 2385-2393 (2009).
- 678 36. S. Doose, H. Neuweiler, M. Sauer, Fluorescence quenching by photoinduced electron transfer: a  
679 reporter for conformational dynamics of macromolecules. *ChemPhysChem* **10**, 1389-1398 (2009).
- 680 37. H. Chen, E. Rhoades, J. S. Butler, S. N. Loh, W. W. Webb, Dynamics of equilibrium structural  
681 fluctuations of apomyoglobin measured by fluorescence correlation spectroscopy. *Proceedings of*  
682 *the National Academy of Sciences* **104**, 10459-10464 (2007).
- 683 38. S. Mukhopadhyay, R. Krishnan, E. A. Lemke, S. Lindquist, A. A. Deniz, A natively unfolded yeast  
684 prion monomer adopts an ensemble of collapsed and rapidly fluctuating structures. *Proceedings of*  
685 *the National Academy of Sciences* **104**, 2649-2654 (2007).
- 686 39. H. Blom, A. Chmyrov, K. Hassler, L. M. Davis, J. Widengren, Triplet-State Investigations of  
687 Fluorescent Dyes at Dielectric Interfaces Using Total Internal Reflection Fluorescence Correlation  
688 Spectroscopy. *The Journal of Physical Chemistry A* **113**, 5554-5566 (2009).
- 689 40. L. J. Lapidus, W. A. Eaton, J. Hofrichter, Measuring the rate of intramolecular contact formation  
690 in polypeptides. *Proceedings of the National Academy of Sciences* **97**, 7220-7225 (2000).
- 691 41. F. Krieger, B. Fierz, O. Bieri, M. Drewello, T. Kiefhaber, Dynamics of unfolded polypeptide chains  
692 as model for the earliest steps in protein folding. *Journal of molecular biology* **332**, 265-274 (2003).
- 693 42. J. K. Lum, H. Neuweiler, A. R. Fersht, Long-range modulation of chain motions within the  
694 intrinsically disordered transactivation domain of tumor suppressor p53. *Journal of the American*  
695 *Chemical Society* **134**, 1617-1622 (2012).
- 696 43. R. R. Goluguri, S. Sen, J. Udgaonkar, Microsecond sub-domain motions and the folding and  
697 misfolding of the mouse prion protein. *eLife* **8**, e44766 (2019).
- 698 44. S. Sen, H. Kumar, J. B. Udgaonkar, Microsecond Dynamics During the Binding-induced Folding  
699 of an Intrinsically Disordered Protein. *Journal of Molecular Biology* **433**, 167254 (2021).

- 700 45. S. A. Waldauer, O. Bakajin, L. J. Lapidus, Extremely slow intramolecular diffusion in unfolded  
701 protein L. *Proceedings of the National Academy of Sciences* **107**, 13713-13717 (2010).
- 702 46. E. Sisamakias, A. Valeri, S. Kalinin, P. J. Rothwell, C. A. Seidel, Accurate single-molecule FRET  
703 studies using multiparameter fluorescence detection. *Methods in enzymology* **475**, 455-514 (2010).
- 704 47. S. Kalinin *et al.*, A toolkit and benchmark study for FRET-restrained high-precision structural  
705 modeling. *Nature Methods* **9**, 1218-1225 (2012).
- 706 48. B. Schuler, W. A. Eaton, Protein folding studied by single-molecule FRET. *Current opinion in*  
707 *structural biology* **18**, 16-26 (2008).
- 708 49. A. Borgia, P. M. Williams, J. Clarke, Single-molecule studies of protein folding. *Annu. Rev.*  
709 *Biochem.* **77**, 101-125 (2008).
- 710 50. I. V. Gopich, A. Szabo, Theory of the energy transfer efficiency and fluorescence lifetime  
711 distribution in single-molecule FRET. *Proceedings of the National Academy of Sciences* **109**, 7747-  
712 7752 (2012).
- 713 51. B. Schuler, Perspective: Chain dynamics of unfolded and intrinsically disordered proteins from  
714 nanosecond fluorescence correlation spectroscopy combined with single-molecule FRET. *The*  
715 *Journal of Chemical Physics* **149**, 010901 (2018).
- 716 52. A. Barth *et al.*, Unraveling multi-state molecular dynamics in single-molecule FRET experiments-  
717 Part I: Theory of FRET-Lines. arxiv:2107.14770 (2021).
- 718 53. H. Hofmann *et al.*, Polymer scaling laws of unfolded and intrinsically disordered proteins  
719 quantified with single-molecule spectroscopy. *Proceedings of the National Academy of Sciences*  
720 **109**, 16155-16160 (2012).
- 721 54. C. Igraja, D. Peter, C. Weiler, E. Izaurralde, 4E-BPs require non-canonical 4E-binding motifs and  
722 a lateral surface of eIF4E to repress translation. *Nature communications* **5**, 1-14 (2014).
- 723 55. Y. Li, R. V. Shivnaraine, F. Huang, J. W. Wells, C. C. Gradinaru, Ligand-Induced Coupling  
724 between Oligomers of the M<sub>2</sub> Receptor and the G<sub>i1</sub> Protein in Live Cells. *Biophysical Journal* **115**,  
725 881-895 (2018).
- 726 56. D. Badali, C. C. Gradinaru, The effect of Brownian motion of fluorescent probes on measuring  
727 nanoscale distances by Förster resonance energy transfer. *The Journal of Chemical Physics* **134**,  
728 225102 (2011).
- 729 57. E. Haustein, P. Schwille, Fluorescence Correlation Spectroscopy: Novel Variations of an  
730 Established Technique. *Annual Review of Biophysics and Biomolecular Structure* **36**, 151-169  
731 (2007).
- 732 58. A. Mazouchi, B. Liu, A. Bahram, C. C. Gradinaru, On the performance of bioanalytical  
733 fluorescence correlation spectroscopy measurements in a multiparameter photon-counting  
734 microscope. *Anal Chim Acta* **688**, 61-69 (2011).
- 735 59. H. J. Feldman, C. W. Hogue, Probabilistic sampling of protein conformations: new hope for brute  
736 force? *Proteins: Structure, Function, and Bioinformatics* **46**, 8-23 (2002).
- 737 60. M. Dimura *et al.*, Quantitative FRET studies and integrative modeling unravel the structure and  
738 dynamics of biomolecular systems. *Current opinion in structural biology* **40**, 163-185 (2016).

739

740